Supplementary Information

Gold-functionalized Organosilica Nanoparticles Reveal Cell Fusion-Associated Adaptive Responses after Nanoradiosensitization of Melanoma Cells

Michihiro Nakamura [1,2], Junna Nakamura [1,2], Yasuo Shiohama [1,2], Tomohiro Haruta[3], Kei-ichi Fukunaga [3], Haruka Murayama [3], Masaya Igase [4], Takuya Mizuno [4], Tetsu Yonezawa [5,6]*

[1] Department of Organ Anatomy and Nanomedicine, Yamaguchi University Graduate School of Medicine, 1-1-1 Minami-Kogushi, Ube, Yamaguchi 755-8505, Japan

[2] Research Institute for Cell Design Medical Science, Yamaguchi University, 1-1-1 Minami-Kogushi, Ube, Yamaguchi 755-8505, Japan

[3] Solution Planning Department, Solution Development Center, JEOL Ltd., Akishima, Tokyo, 196-8558, Japan

[4] Laboratory of Molecular Diagnostics and Therapeutics, Joint Faculty of Veterinary Medicine, Yamaguchi University, Yamaguchi, Japan

[5] Division of Materials Science and Engineering, Faculty of Engineering, Hokkaido University, Kita 13 Nishi 8, Kita-ku, Sapporo, Hokkaido 060-8628, Japan

[6] Department of Chemical Engineering, Faculty of Engineering, Chulalongkorn University, 254 Phaya Thai Rd, Wang Mai, Pathum Wan, Bangkok 10330, Thailand

* Correspondence: Michihiro Nakamura, nakam@yamaguchi-u.ac.jp

Supporting Figures

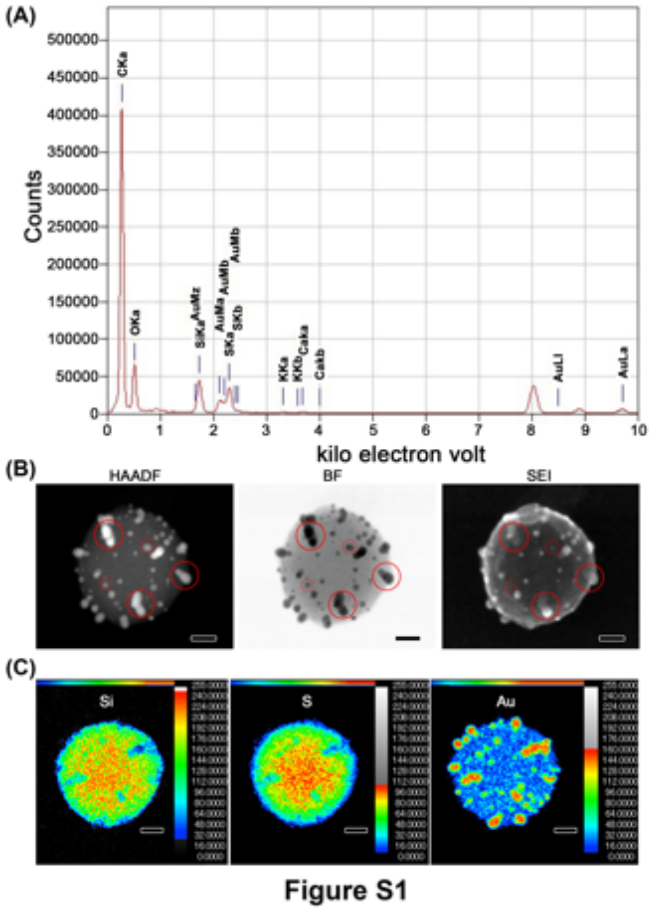

Figure S1

Figure S1. Additional structural characterization of gold-functionalized thiol-organosilica nanoparticles (OSAu).

(A) Scanning electron microscopy–energy-dispersive X-ray spectroscopy (SEM–EDX) analysis of OSAu showing the presence of silicon (Si), oxygen (O), sulfur (S), and gold (Au), confirming the coexistence of the organosilica framework and gold nanostructures within the hybrid particles. (B) High-angle annular dark-field scanning transmission electron microscopy (HAADF-STEM) and secondary electron intensity (SEI) images of OSAu. HAADF-STEM highlights Au-rich regions because of the high atomic number of Au, whereas SEI provides complementary surface-

sensitive information. Some surface-associated gold nanoparticles exhibiting reduced contrast in SEI images are indicated by red circles. Scale bars represent 20 nm. (C) Elemental mapping images of Si, S, and Au. Si and S signals are broadly distributed throughout the spherical organosilica matrix, whereas Au signals appear as discrete surface-associated domains, supporting heterogeneous formation of gold nanostructures on the particle surface. The merged elemental map enables clear discrimination between the thiol-organosilica matrix and gold nanostructures and further supports the structural heterogeneity of OSAu. Such heterogeneity in gold size and interfacial morphology is expected to influence nano–bio interactions and local responses during irradiation.

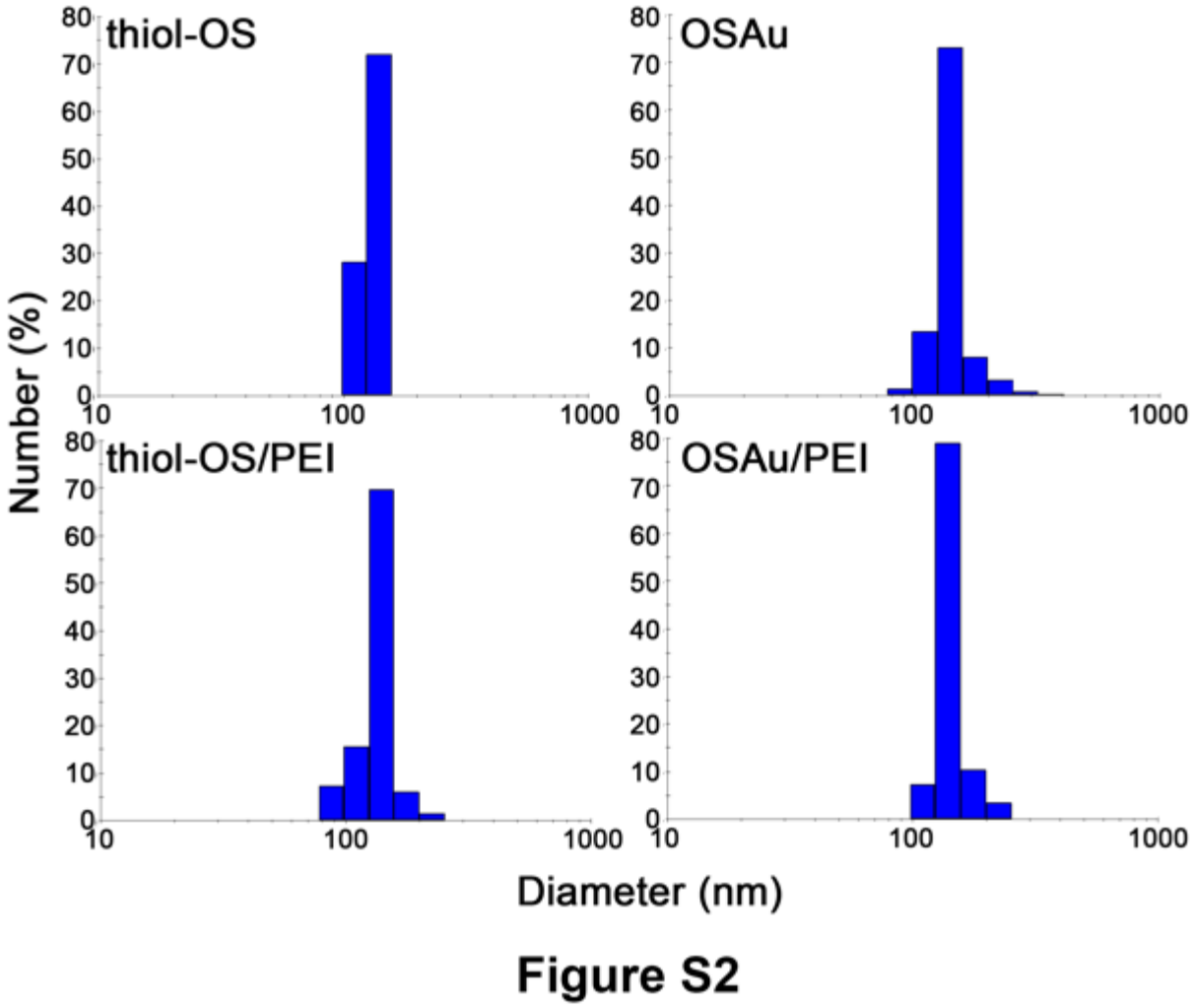

Figure S2

Figure S2. Hydrodynamic size distribution of thiol-OS, OSAu, thiol-OS/PEI, and OSAu/PEI measured by dynamic light scattering.

Representative dynamic light scattering (DLS) histograms of thiol-OS, OSAu, thiol-OS/PEI, and OSAu/PEI. All nanoparticle preparations showed relatively narrow size distributions with single major peaks, indicating monodisperse or near-monodisperse dispersions under the measurement conditions. The increase in hydrodynamic diameter after PEI functionalization is consistent with the formation of a hydrated polymer layer on the particle surface. This surface expansion is also

consistent with the enhanced interaction of OSAu/PEI with cell membranes observed in subsequent cellular analyses.

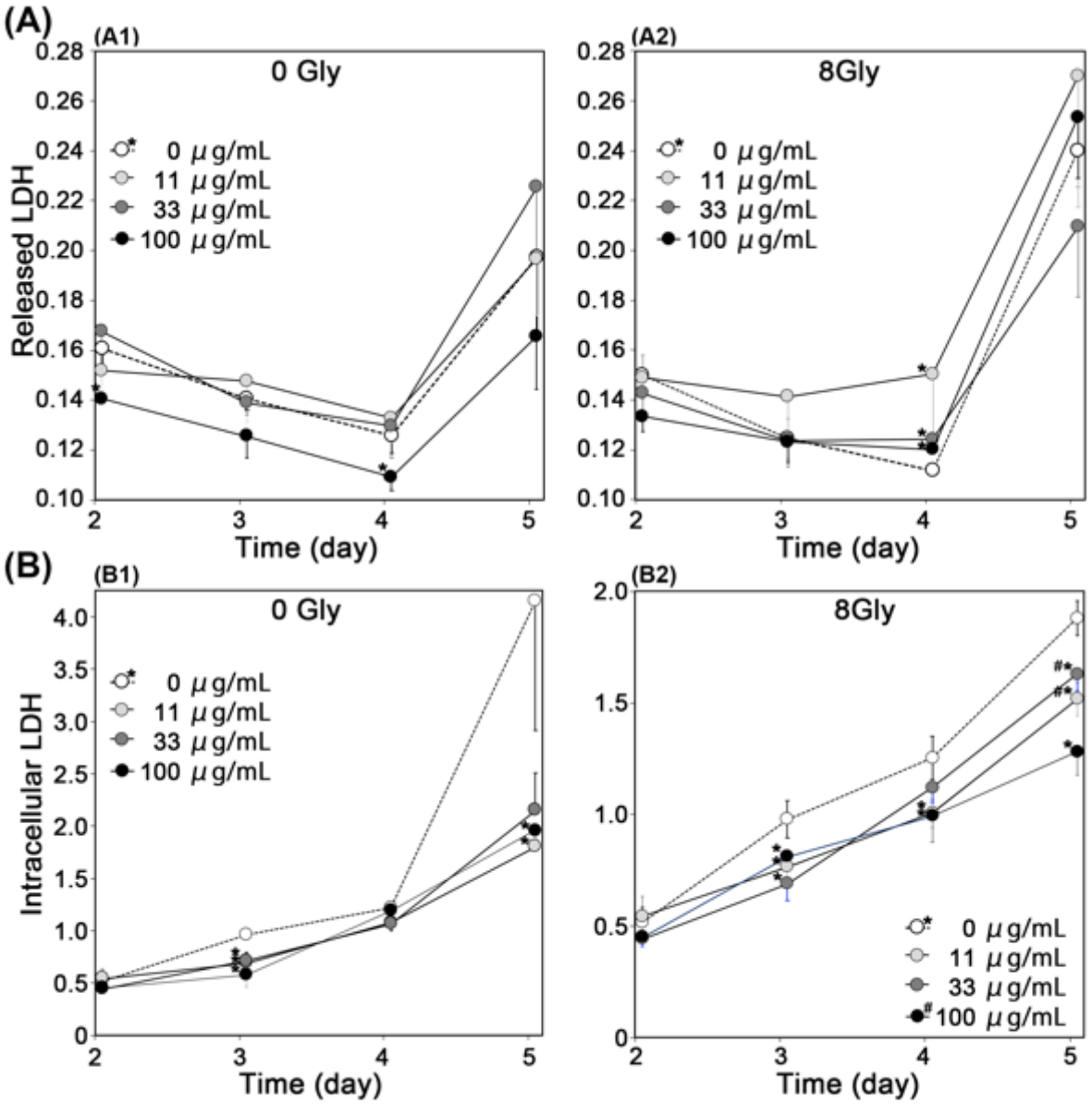

Figure S3

Figure S3. Evaluation of lactate dehydrogenase (LDH) activity in B16F10 cells treated with OSAu/PEI and irradiation.

Evaluation of LDH activity in the culture medium (released LDH; A1, A2) and cell lysates (intracellular LDH; B1, B2) of nonirradiated B16F10 cells (A1, B1) and irradiated cells (A2, B2) treated with various concentrations of OSAu/PEI. Released LDH reflects extracellular leakage associated with membrane damage, whereas intracellular LDH reflects residual metabolic and biosynthetic activity. Compared with released LDH, intracellular LDH more clearly reflected the suppressive effects of nanoirradiation on cell viability and cellular function. Notably, the decrease in intracellular LDH was observed without a corresponding marked increase in released LDH, suggesting that the effect primarily reflects reduced intracellular LDH content, consistent with reduced viable cell function and cellular functional decline rather than simple membrane rupture or acute leakage. These results suggest that early membrane leakage alone does not fully capture the effects of nanoirradiation and that intracellular LDH provides a more sensitive measure of treatment-induced functional decline under the present conditions.

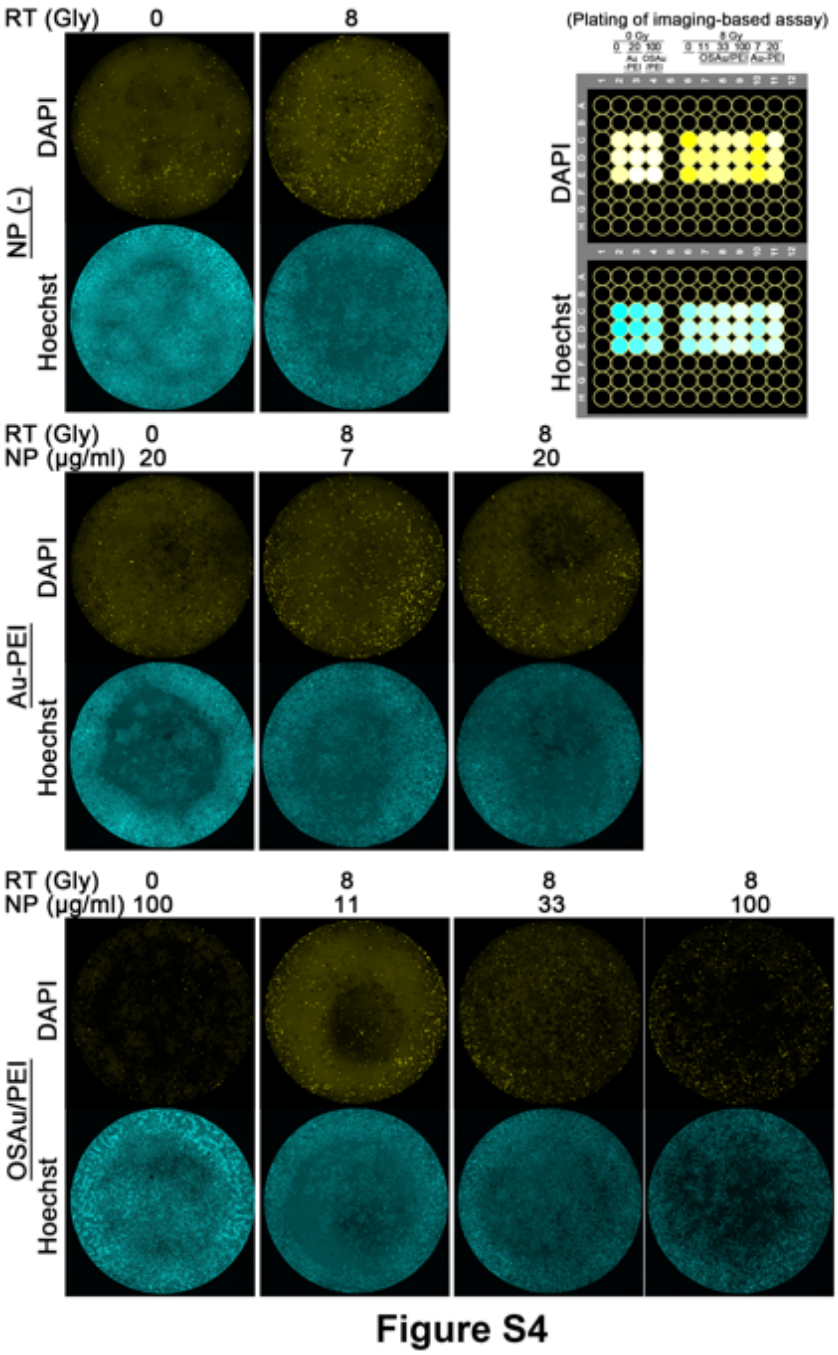

Figure S4

Figure S4. Nuclear imaging of irradiated cells in individual wells of a 96-well plate on day 5.

Fluorescence microscopy imaging of B16F10 cells treated with various concentrations of Au-PEI (0, 7, and 20 μg/mL) or OSAu/PEI (0, 11, 33, and 100 μg/mL) and irradiated with 0 or 8 Gy. On day 5, nuclei were stained with DAPI (yellow) and Hoechst (cyan). Representative images of

individual wells and the overall plate layout are shown. These images provide additional visual support for the nuclear imaging-based analyses presented in Figure 4 and illustrate treatment-dependent differences in nuclear density, nuclear fragmentation, and the appearance of enlarged nuclei. In particular, the reduced density of nuclei and the coexistence of fragmented and enlarged nuclear structures indicate that nanoirradiation induces both cell death-associated and potential adaptive nuclear phenotypes within the same population. These well-level images also highlight an advantage of the imaging-based assay, namely its ability to directly visualize treatment-dependent changes in nuclear density and morphology that may not be fully captured by metabolic readouts alone.

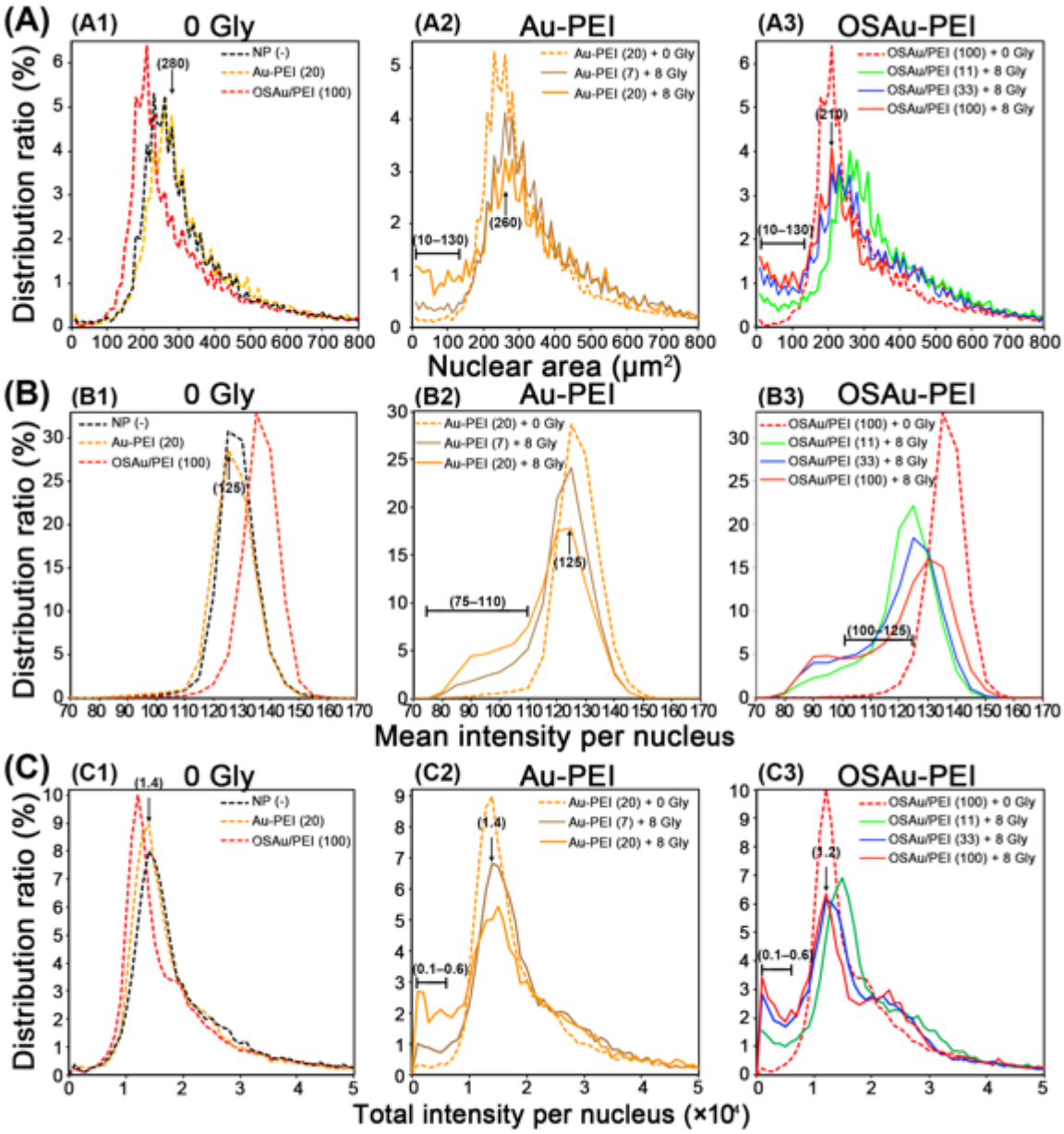

Figure S5

Figure S5. Distribution of nuclear fluorescence parameters in nonirradiated cells and cells treated with Au-PEI or OSAu/PEI.

(A1–A3) Distribution of nuclear area in nonirradiated cells (A1) and cells treated with Au-PEI (A2) or OSAu/PEI (A3).

(B1–B3) Distribution of average fluorescence intensity per nucleus in nonirradiated cells (B1) and cells treated with Au-PEI (B2) or OSAu/PEI (B3).

(C1–C3) Distribution of total fluorescence intensity per nucleus in nonirradiated cells (C1) and cells treated with Au-PEI (C2) or OSAu/PEI (C3). Arrows indicate representative peak positions, and horizontal brackets denote the ranges of values highlighted in the main text. These plots provide additional quantitative support for the treatment-dependent shifts in nuclear morphology and fluorescence characteristics. In particular, irradiation broadened the distributions and increased the proportion of nuclei with smaller area and lower fluorescence intensity, indicating heterogeneous nuclear responses associated with reduced nuclear fluorescence signal and altered nuclear morphology. These shifts were further enhanced in nanoparticle-treated cells, especially in the OSAu/PEI group, supporting a redistribution of the nuclear population toward smaller, low-intensity nuclei at the single-nucleus level. At the same time, the persistence of broader distributions with tails extending toward larger nuclei indicates the coexistence of enlarged nuclear populations that may correspond to senescence- or polyploidization-related states.

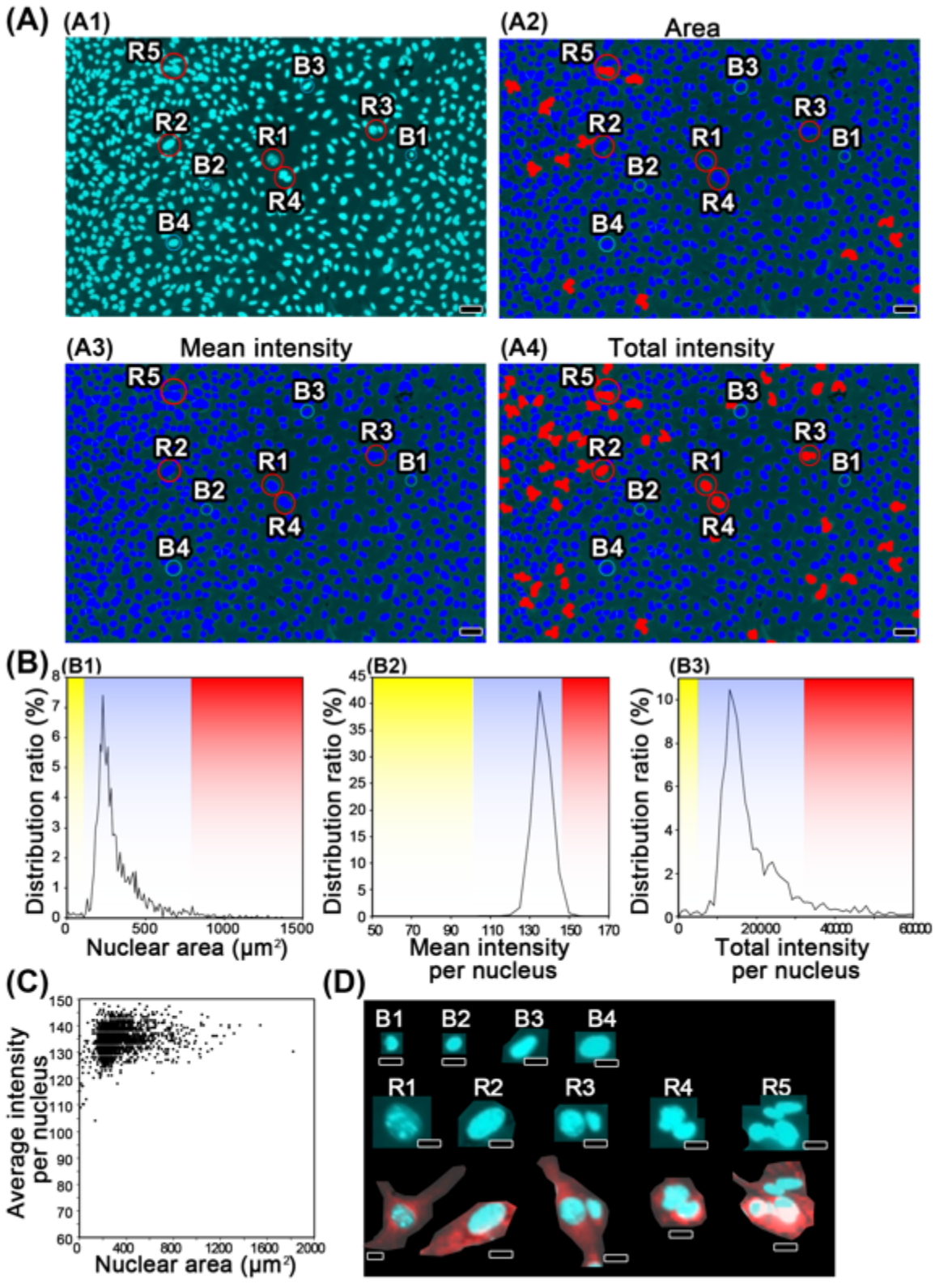
(A)
(A1)
(A2)
Area
(A3)
Mean intensity
(A4)
Total intensity
R5
B3
R3
R2
R1
B1
B2
R4
B4
(B)
(B1)
(B2)
(B3)
Distribution ratio (%)
Nuclear area (μm²)
Mean intensity per nucleus
Total intensity per nucleus
(C)
Average intensity per nucleus
Nuclear area (μm²)
(D)
B1
B2
B3
B4
R1
R2
R3
R4
R5

Figure S6a

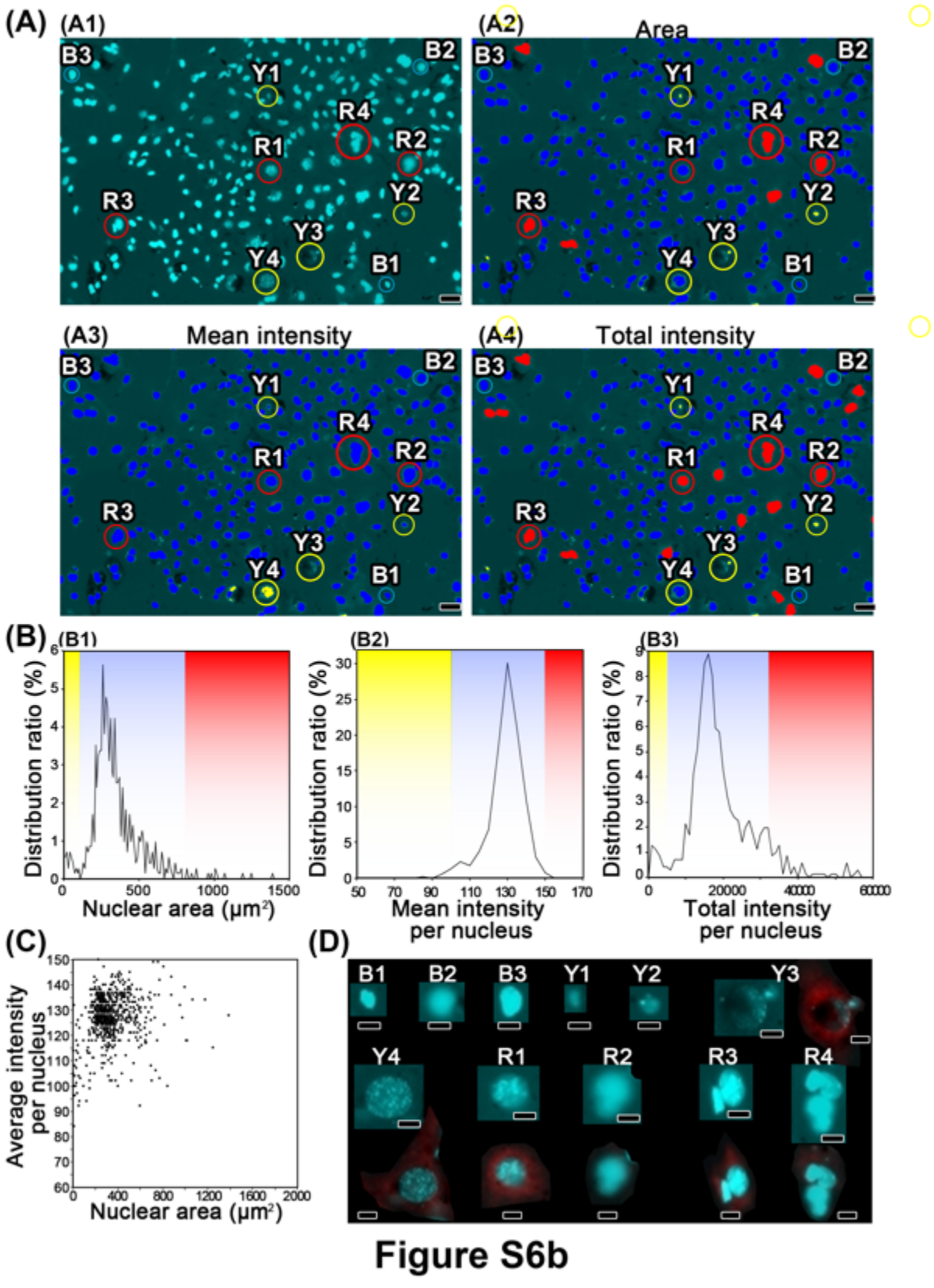
(A)
(A1)
(A2)
Area
(A3)
Mean intensity
(A4)
Total intensity
B1
B2
B3
Y1
Y2
Y3
Y4
R1
R2
R3
R4
(B)
(B1)
(B2)
(B3)
Distribution ratio (%)
Nuclear area (μm²)
Mean intensity per nucleus
Total intensity per nucleus
(C)
Average intensity per nucleus
Nuclear area (μm²)
(D)

Figure S6b

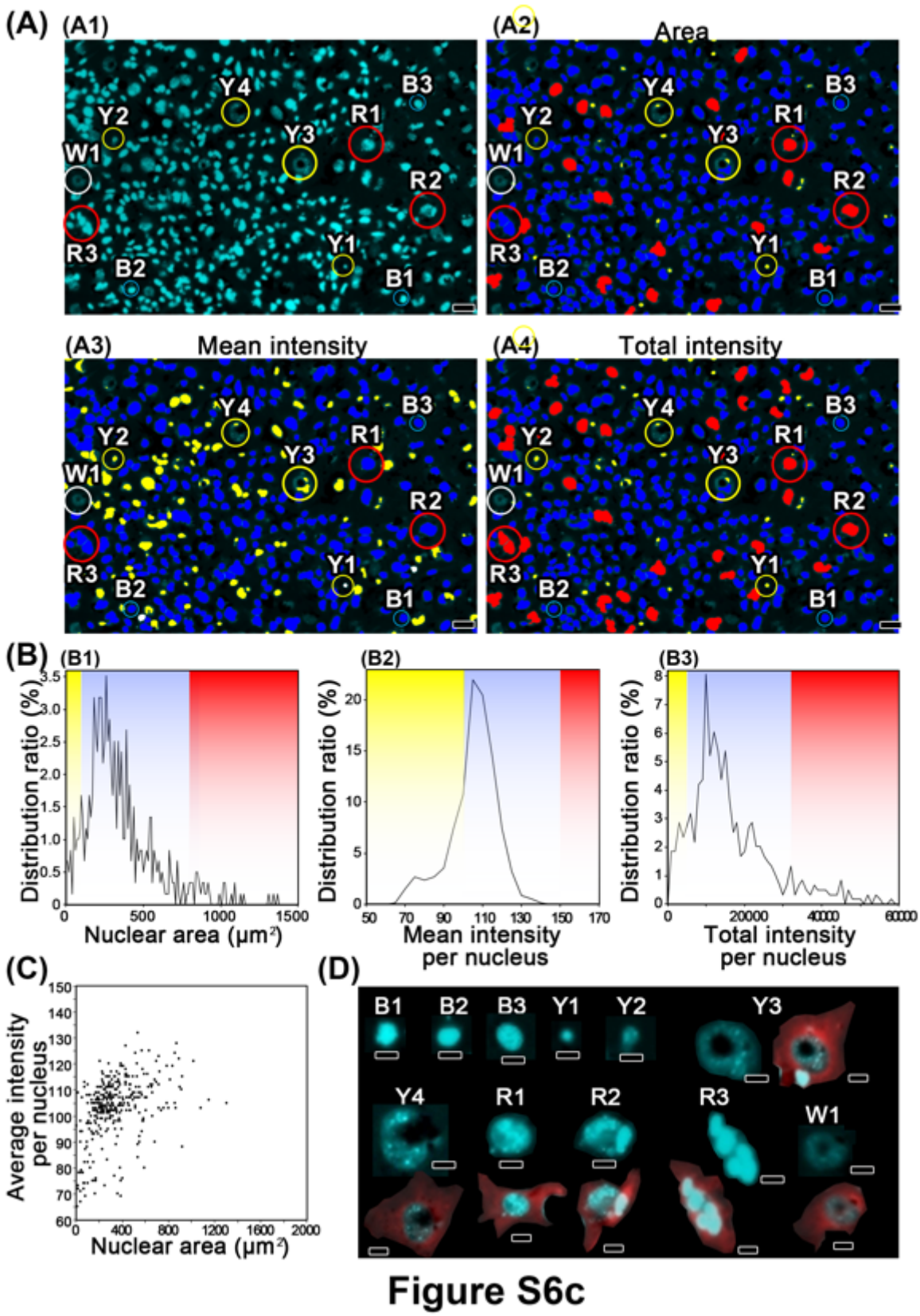
(A)
(A1)
(A2)
Area
(A3)
Mean intensity
(A4)
Total intensity
Y4
B3
Y2
R1
Y3
W1
R2
R3
Y1
B2
B1
(B)
(B1)
(B2)
(B3)
Distribution ratio (%)
Nuclear area (μm²)
Mean intensity per nucleus
Total intensity per nucleus
(C)
Average intensity per nucleus
Nuclear area (μm²)
(D)
B1
B2
B3
Y1
Y2
Y3
Y4
R1
R2
R3
W1

Figure S6c

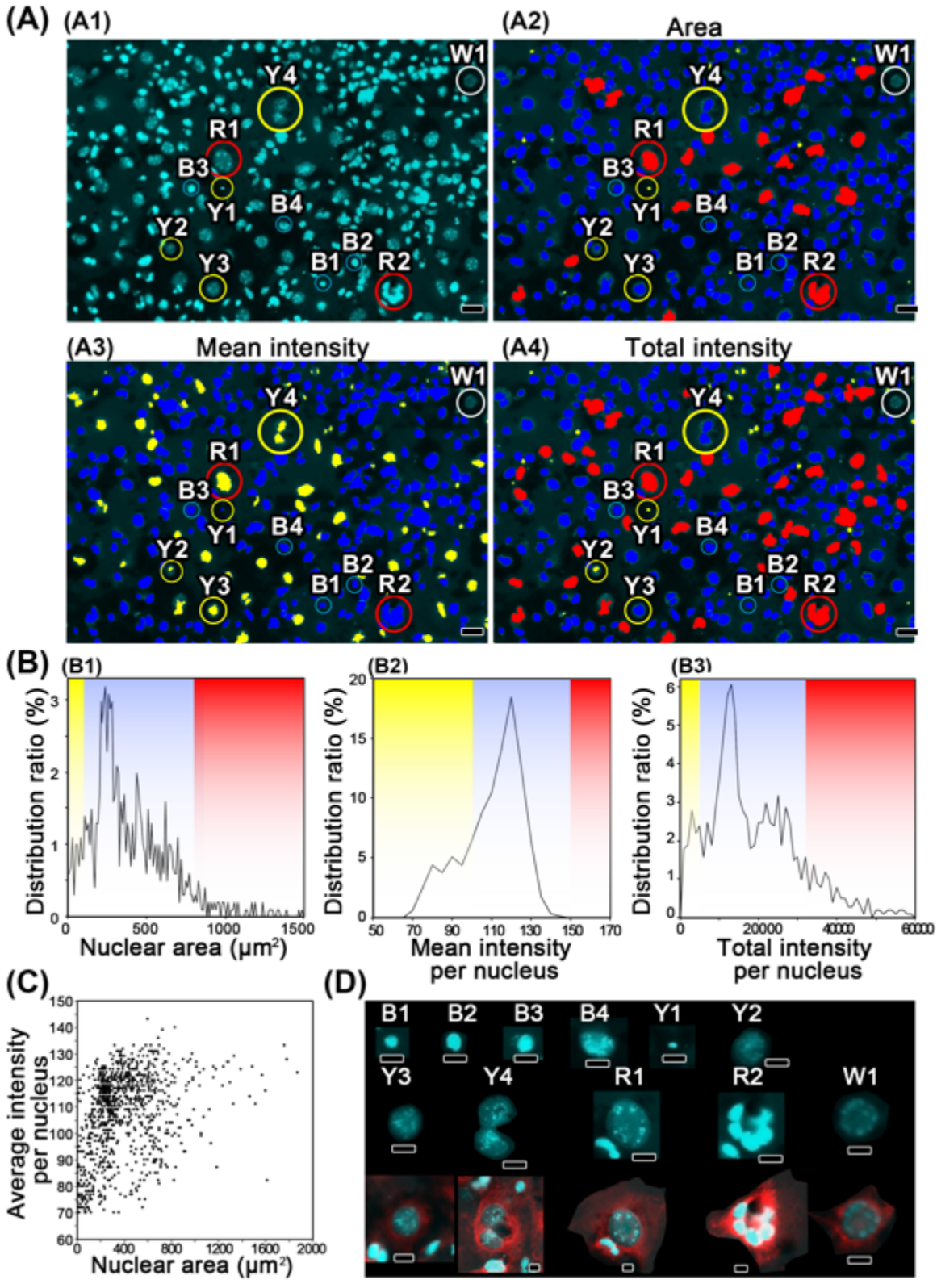
(A)
(A1)
(A2)
Area
(A3)
Mean intensity
(A4)
Total intensity
W1
Y4
R1
B3
Y1
B4
Y2
B2
Y3
B1
R2
(B)
(B1)
(B2)
(B3)
Distribution ratio (%)
Nuclear area (μm²)
Mean intensity per nucleus
Total intensity per nucleus
(C)
Average intensity per nucleus
Nuclear area (μm²)
(D)
B1
B2
B3
B4
Y1
Y2
Y3
Y4
R1
R2
W1

Figure S6d

Figure S6. Morphological evaluation of irradiated cells and segmentation-based classification of nuclei.

Nuclei of nonirradiated cells (S6a), irradiated cells without nanoparticle treatment (S6b), irradiated cells treated with 20 μg/mL Au-PEI (S6c), and irradiated cells treated with 100 μg/mL OSAu/PEI (S6d) were analyzed by fluorescence microscopy. (A) Fluorescence microscopy images of nuclei stained with Hoechst (cyan) (A1), together with segmentation results based on nuclear size (A2), average fluorescence intensity (A3), and total fluorescence intensity (A4). Nuclei were classified into small/low (yellow), medium (blue), and large/high (red) groups. These panels provide a visual overview of how irradiation and nanoparticle treatment altered nuclear morphology and signal intensity, including increased frequencies of small or weakly fluorescent nuclei and the persistence of enlarged nuclei in treated populations. Scale bar, 50 μm. (B) Distributions of nuclear area (B1), average fluorescence intensity per nucleus (B2), and total fluorescence intensity per nucleus (B3). These plots quantitatively show treatment-dependent redistribution of nuclei, with irradiation shifting the population toward smaller nuclear area and lower fluorescence intensity, and with OSAu/PEI further enhancing this shift compared with irradiation alone or Au-PEI treatment. (C) Scatter plots showing the relationship between nuclear area and average fluorescence intensity of individual nuclei. These plots illustrate that irradiation and nanoradiosensitization did not simply reduce nuclear parameters uniformly, but generated heterogeneous and partially separable nuclear subpopulations, including small/low-intensity nuclei, intermediate nuclei, and enlarged/high-intensity nuclei. (D) Representative images of single nuclei segmented in panel A and classified as small/low (Y), medium (B), and large/high (R). Some nuclei are shown together with counterstained mitochondria using TMRE. These images provide morphological confirmation of the segmented classes and illustrate the

coexistence of fragmented nuclei, reduced-fluorescence nuclei, enlarged nuclei, and multinucleated structures after irradiation and nanoradiosensitization. Scale bar, 25 μm. Together, these analyses provide supplementary evidence that irradiation and nanoparticle treatment induced a broad spectrum of nuclear phenotypes at the single-cell level, rather than a simple binary shift between viable and nonviable states, and support the interpretation that OSAu/PEI promotes a pronounced redistribution toward small, low-intensity nuclei while preserving a subset of enlarged nuclei associated with adaptive stress responses.

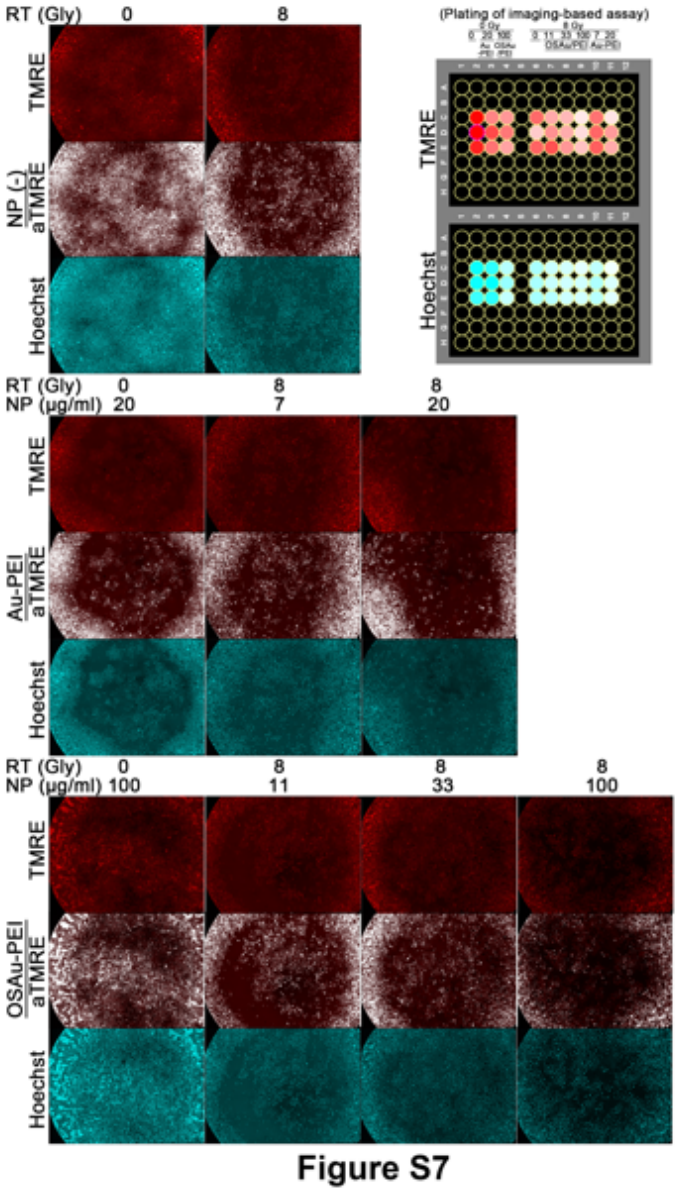

Figure S7

Figure S7. Imaging of mitochondria and nuclei of irradiated cells in individual wells of a 96-well plate on day 5.

Fluorescence microscopy imaging of B16F10 cells treated with various concentrations of Au-PEI (0, 7, and 20 μg/mL) or OSAu/PEI (0, 11, 33, and 100 μg/mL) and irradiated with 0 or 8 Gy. On day 5, mitochondria and nuclei were stained with TMRE (red) and Hoechst (cyan), respectively. The analyzed mitochondrial regions are shown in white (TMRE). Representative images of

individual wells and the overall plate layout are shown. These images provide additional visual support for the mitochondria–nucleus correlation analysis presented in Figure 5. The marked variability in TMRE fluorescence indicates that mitochondrial responses were heterogeneous even within the same treatment group, consistent with the presence of cells with distinct TMRE-based mitochondrial signal states after irradiation.

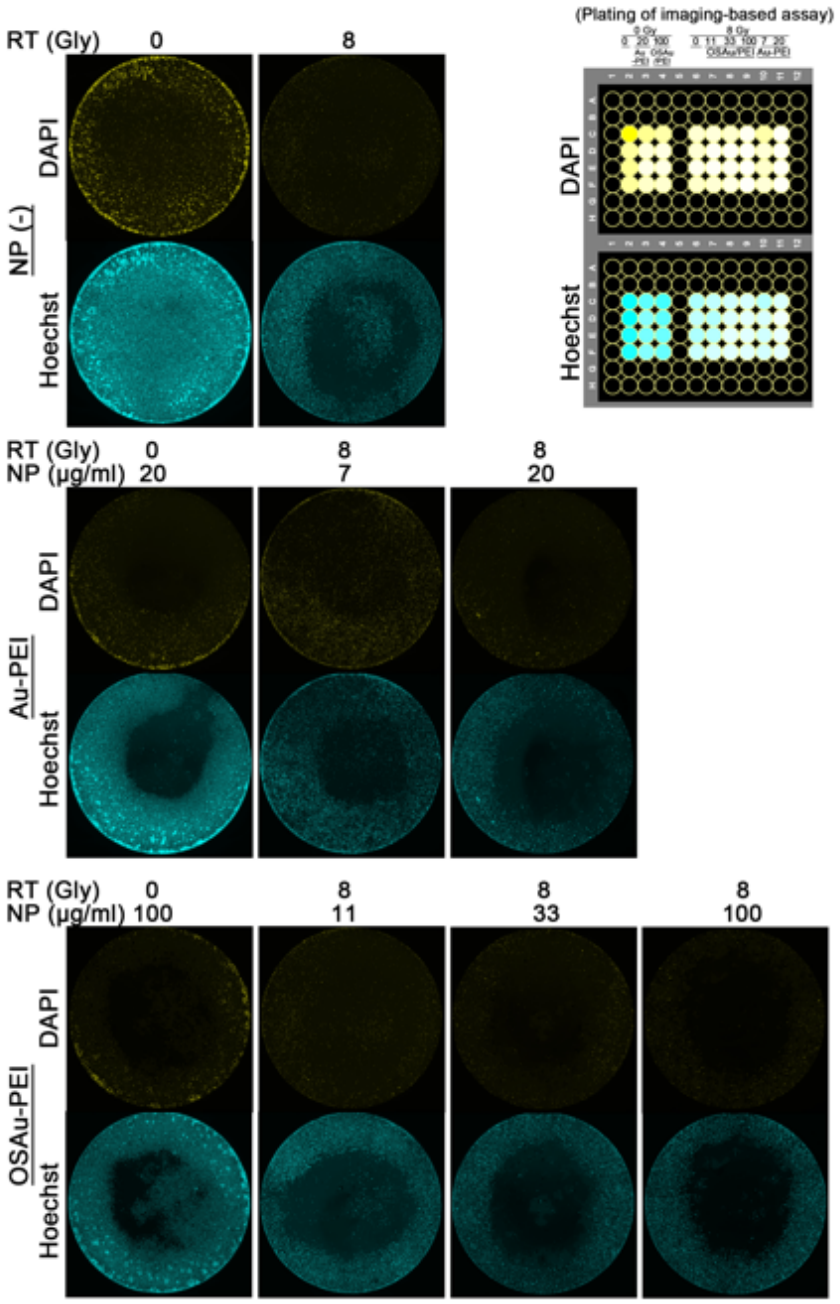

Figure S8

Figure S8. Nuclear imaging of irradiated cells in individual wells of a 96-well plate on day 11.

Fluorescence microscopy imaging of B16F10 cells treated with various concentrations of Au-PEI (0, 7, and 20 μg/mL) or OSAu/PEI (0, 11, 33, and 100 μg/mL) and irradiated with 0 or 8 Gy. On day 11, nuclei were stained with DAPI (yellow) and Hoechst (cyan). Compared with day 5, these images show reduced cell density, increased heterogeneity in nuclear morphology, and persistence of a subset of surviving cells, thereby supporting the long-term nuclear analyses presented in Figure 6. The remaining cells exhibited a mixture of abnormal enlarged nuclei, weakly stained nuclei, and smaller surviving nuclei, indicating that long-term residual cells were morphologically diverse.

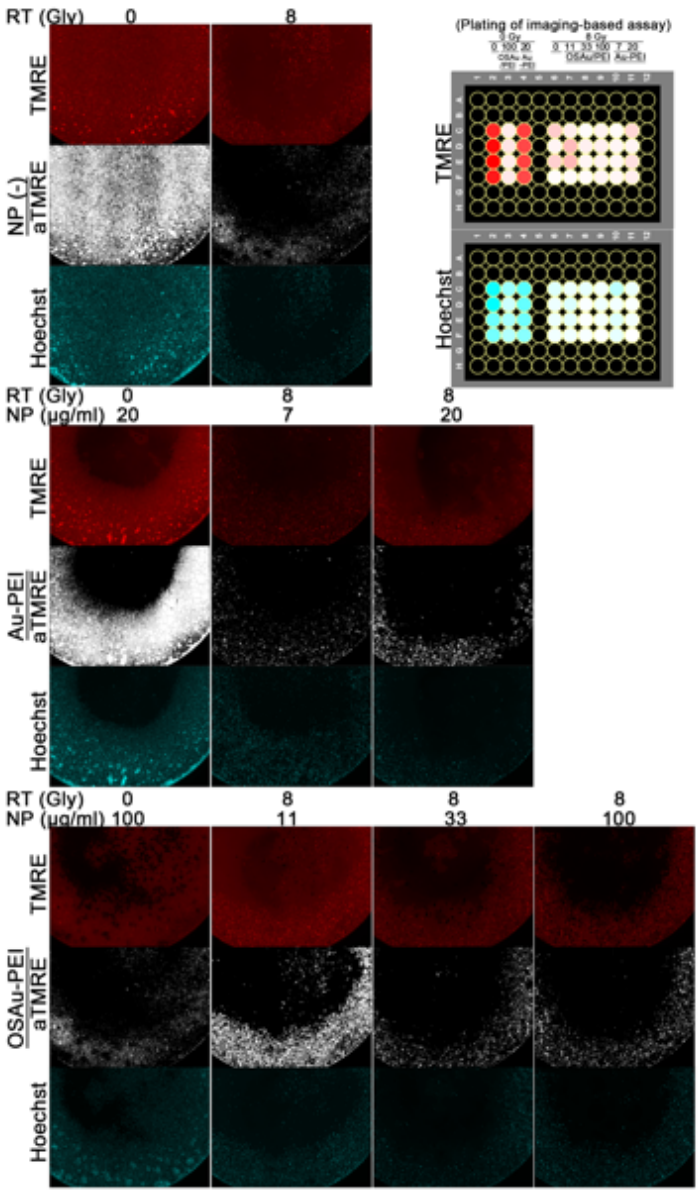

Figure S9

Figure S9. Imaging of mitochondria and nuclei of irradiated cells in individual wells of a 96-well plate on day 11.

Fluorescence microscopy imaging of B16F10 cells treated with various concentrations of Au-PEI (0, 7, and 20 μg/mL) or OSAu/PEI (0, 11, 33, and 100 μg/mL) and irradiated with 0 or 8 Gy. On

day 11, mitochondria and nuclei were stained with TMRE (red) and Hoechst (cyan), respectively. The analyzed mitochondrial regions are shown in white (aTMRE). These images illustrate heterogeneous long-term mitochondrial responses among surviving cells and complement the quantitative mitochondrial analyses shown in Figure 6. In particular, some cells retained strong TMRE fluorescence despite marked nuclear abnormalities or reduced cell density, suggesting persistence of residual subpopulations retaining TMRE-based mitochondrial signals at later time points.

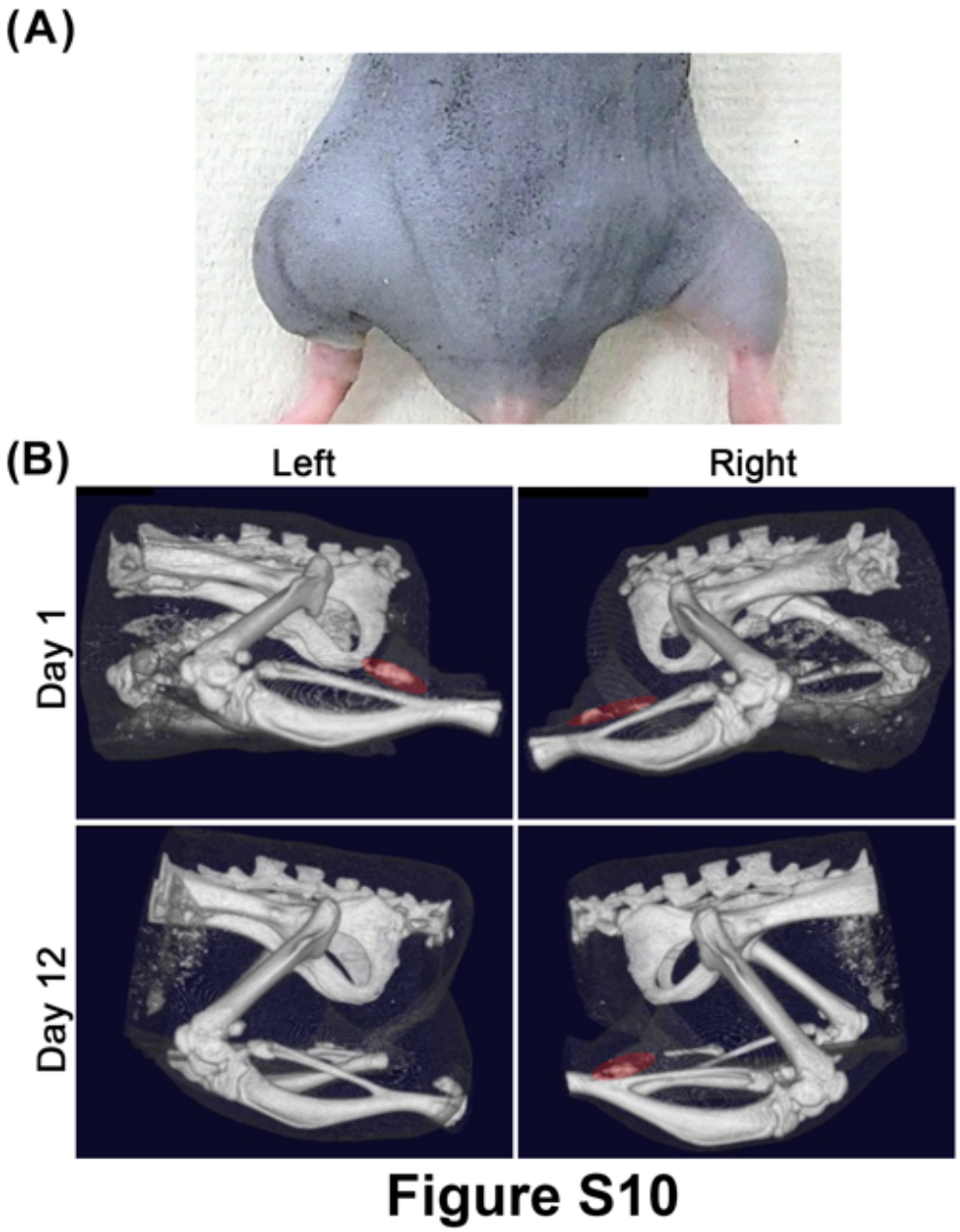

Figure S10

Figure S10. X-ray CT analysis of a tumor-bearing mouse subjected to X-ray irradiation.

The hind legs of mice were subcutaneously implanted with B16F10 cells pretreated with 100 μg/mL OSAu/PEI on day 0, followed by X-ray irradiation of only the right leg at 10 Gy one day after implantation. This experiment was performed as an additional condition-evaluation study at a different irradiation dose from that used in the main in vivo experiment shown in Figure 8 (6

Gy), and is presented here to illustrate nanoparticle retention and CT visibility under a more strongly growth-suppressive condition. Both hind legs were photographed on day 12 (A) and imaged using X-ray CT on days 1 and 12 (B). Tumor masses containing OSAu/PEI-treated cells were visualized in both hind legs on day 1 and only in the irradiated right leg on day 12. Tumor regions containing nanoparticles are highlighted in transparent red. These data support the interpretation that irradiated, growth-suppressed tumor tissue retained stronger nanoparticle-associated CT signals. The findings further support the utility of OSAu/PEI as a theranostic platform combining radiosensitization and X-ray-based visualization.

Supporting Tables

Table S1. Flow cytometric analysis of nanoparticle uptake in B16F10 cells treated with OSAu/PEI.

Flow cytometric analysis of B16F10 cells treated with increasing concentrations of OSAu/PEI. The percentage of nanoparticle-positive cells (Population), mean fluorescence intensity (Level, F.I.), and coefficient of variation (CV) of fluorescence intensity are shown. The high proportion of positive cells indicates that OSAu/PEI associated with the majority of the cell population even at the lowest concentration tested. The concentration-dependent increase in fluorescence intensity suggests increased nanoparticle binding and/or uptake at higher concentrations. The relatively large CV values indicate that nanoparticle-associated fluorescence was not uniform across the population, supporting the single-cell heterogeneity observed by fluorescence microscopy. Each value represents the mean ± SD of three replicates.

Particle Conc. (μg/mL)	Population (%)	Level (F.I.)	CV (%) of F.I.
0	0.0	0.0	45.9 ± 8.9
11	96.3 ± 0.4	122.4 ± 10.2	61.6 ± 4.0
33	94.1 ± 2.0	177.8 ± 7.5	66.3 ± 5.3
100	95.9 ± 2.0	258.9 ± 56.9	75.5 ± 13.4

Each value represents the mean ± SD of 3 replicates

Table S2. Criteria used for subset analysis and segmentation-based classification of nuclear imaging data.

Criteria used for the classification of nuclei in the imaging-based subset analysis shown in Figure S6. Nuclei were grouped into small, middle, and large categories according to nuclear area, average fluorescence intensity, and total fluorescence intensity. This classification enabled comparison of nuclei with reduced size or fluorescence, nuclei with intermediate characteristics, and enlarged or highly fluorescent nuclei across treatment groups. These thresholds were empirically selected to assist in the interpretation of irradiation- and nanoparticle-induced nuclear heterogeneity and to provide a structured framework for representative image selection and segmentation-based analysis. The classification was intended for descriptive comparison of image-derived nuclear phenotypes rather than for strict assignment of fixed biological states.

	Small	Middle	Large
Area (μm^2)	< 100	100–800	800 <
Average fluorescence intensity	< 100	100–150	150 <
Total fluorescence intensity	< 5000	5000–32000	32000 <

Supplementary Notes

Supplementary Note 1. Detailed observations from time-lapse imaging (Movies 4A–4E)

Long-term time-lapse imaging was performed to visualize the dynamic cellular responses of B16F10 melanoma cells after nanoirradiation with OSAu/PEI. These movies provide additional temporal detail for the representative events summarized in Figure 7B and reveal sequential relationships among senescence-like enlargement, multinucleation, cell fusion, mitochondrial transfer-associated phenomena, and the emergence of residual progeny-like cells.

In Movie 4A, senescence-associated morphological changes became evident several days after irradiation. Nuclear enlargement was first detectable at approximately 3 days and 12 h after irradiation, and by day 5 some cells exhibited marked nuclear expansion and enlarged cytoplasmic morphology. A subset of these enlarged cells subsequently disappeared after transient increases in TMRE fluorescence, whereas others remained visible for extended periods and later developed multinucleation. In some cases, multinucleated daughter-like structures appeared after apparent division of enlarged or senescent cells, followed by either disappearance or DAPI-positive cell death at later time points. These observations indicate that nanoirradiation induces not only acute cell death but also prolonged senescence-associated cellular remodeling.

Movie 4B provides a representative example of PGCC formation through fusion between normal-sized cells. Two motile cells with strong mitochondrial fluorescence gradually approached one another and established close contact before forming a connected multinucleated structure. This fused structure subsequently exhibited persistent TMRE fluorescence and strong Hoechst-associated nuclear signals. The sequence suggests that direct fusion between morphologically non-

senescent cells can serve as one route for the generation of multinucleated giant cells after nanoirradiation.

Movie 4C shows an additional route of PGCC formation involving a senescent-like cell and surrounding neighboring cells. An enlarged senescent-like cell became apparent after irradiation, and over time multiple smaller cells accumulated around it. These cells subsequently merged into a multinucleated structure with heterogeneous nuclear morphology and variable fluorescence intensity. Compared with Movie 4B, this sequence suggests that fusion-associated PGCC formation is not restricted to interactions between similarly sized motile cells but may also involve senescent or enlarged cells acting as fusion hubs.

Movie 4D shows the emergence of a distinct surviving cell phenotype after nanoirradiation. In this example, a morphologically altered cell underwent further shape change and then produced daughter-like cells with different appearances and mitochondrial signal intensities. One daughter-like structure developed into a larger abnormal cell and disappeared at a later time point, whereas another remained as a smaller viable cell with persistent mitochondrial fluorescence. These observations are consistent with the interpretation that some multinucleated or enlarged cells may give rise to surviving progeny with distinct morphological and metabolic properties.

Movie 4E illustrates tunneling nanotube-associated mitochondrial transfer and formation of vesicle-like mitochondrial structures. A TMRE-positive tubular structure extended from one cell and later fragmented into multiple small fluorescent bodies. These structures remained in the extracellular space for a period and were subsequently contacted by a neighboring cell through a nanotube-like protrusion, followed by apparent incorporation into the recipient cell. During this process, the donor cell later exhibited nuclear staining consistent with cell death, whereas the

recipient cell remained intact. These observations support the idea that mitochondrial transfer-associated phenomena persist after nanoirradiation and may contribute to intercellular adaptation under stress conditions.

Taken together, Movies 4A–4E demonstrate that the responses of nanoirradiated melanoma cells are highly dynamic and heterogeneous. The events observed include senescence-associated enlargement, multinucleation, fusion between multiple cell types, formation of giant cells, emergence of smaller surviving progeny, and tunneling nanotube-associated transfer of mitochondrial material. These movies therefore provide direct temporal support for the interpretation that nanoirradiation triggers a complex adaptive cellular program in which cell fusion and intercellular communication are prominent components.

Supplementary Note 2. Additional interpretation of CLSEM findings

Correlative light and scanning electron microscopy (CLSEM) was performed to further examine the ultrastructural features of nanoirradiated B16F10 melanoma cells and to compare fluorescence-based cellular identification with their corresponding surface morphology. These analyses provided additional support for the interpretation that many of the enlarged or multinucleated structures observed after nanoirradiation represent fused multicellular assemblies rather than isolated single cells.

In the nonirradiated control group, cells exhibited relatively small spindle-shaped or polymorphic morphologies with limited vertical thickness. In some regions, thin tubular structures connecting adjacent cells were visible by SEM, consistent with nanotube-like structures suggested by

fluorescence imaging. These features indicate that intercellular protrusions are present even in untreated cells, although they appeared relatively limited in extent and complexity.

By contrast, in irradiated cells treated with OSAu/PEI, SEM revealed marked morphological remodeling, including enlarged flattened cells, irregular squamous-like surfaces, and extensive cell spreading. Some giant cells extended over a long cytoplasmic axis and exhibited surface features that were not fully predictable from fluorescence microscopy alone. In these cells, flattening and widening of the cell body likely contributed to the broad polymorphic appearance seen by SEM. These observations support the interpretation that nanoirradiation induces major structural reorganization in addition to nuclear and mitochondrial changes.

One of the key findings of CLSEM was that some structures appearing as single cells by fluorescence microscopy were revealed by SEM to be multicellular fused assemblies. In the region corresponding to cell (a), SEM and CLSEM suggested that multiple flattened cells were closely integrated into a continuous structure, including senescent-like spindle-shaped cells and smaller nuclear elements. Similarly, the region corresponding to cell (b), which appeared by fluorescence microscopy as a PGCC containing multiple nuclei, showed by SEM a more extensive irregular squamous morphology than expected, indicating that this structure was not a simple enlarged cell but part of a broader fused multicellular assembly.

High-magnification analysis of region (b) further revealed layered morphology and associated tubular structures. The left side of the structure appeared partially two-layered, and thin protruding tube-like elements extended from the lower region. Corresponding fluorescence images showed linear TMRE-associated and nanoparticle-associated signals adjacent to these structures, indicating that mitochondria-rich cytoplasmic regions and OSAu/PEI-associated fluorescence

were spatially related to the tubular extensions. These findings support the view that fused cellular assemblies retain structurally complex protrusions that may participate in intercellular connectivity or cytoplasmic remodeling.

Region (c) provided particularly important information for interpreting the emergence of a potentially surviving cell population. By fluorescence microscopy, this structure resembled a relatively normal-sized cell located adjacent to the larger fused assembly. SEM showed an oval protrusion corresponding to a nuclear region and an overall morphology more similar to a compact cell than to the highly flattened structures seen in regions (a) and (b). Hoechst-associated fluorescence was confined to a small vertically oriented nuclear structure, whereas OSAu/PEI-associated fluorescence was localized over the larger protruded region. The apparent dissociation between fluorescence signals and SEM morphology suggests that nanoparticle-associated optical interference or signal attenuation may influence the apparent nuclear image in some cells. At the same time, the SEM image suggested that this smaller structure was not fully continuous with the adjacent giant cell but may instead represent a cell in the process of separation or detachment from the fused multicellular region.

This interpretation is consistent with the time-lapse observations in Figure 7B4 and Movie 4D, in which smaller surviving cells emerged from larger abnormal cellular structures. Thus, the CLSEM data provide ultrastructural support for a model in which enlarged fused assemblies, including senescent-like cells and PGCCs, may serve as transitional structures from which smaller morphologically distinct progeny emerge. Although the identity of these surviving cells cannot be definitively established based on morphology alone, their compact morphology and apparent structural independence distinguish them from the larger flattened senescent-like assemblies.

Taken together, the CLSEM analyses reinforce three major interpretations. First, post-irradiation melanoma cells undergo extensive flattening, spreading, and surface remodeling. Second, many enlarged and multinucleated structures are better interpreted as fused multicellular assemblies than as isolated enlarged cells. Third, compact cell-like structures adjacent to these assemblies may represent surviving progeny emerging from the remodeled post-irradiation population. These findings therefore complement the fluorescence-based and time-lapse observations and provide additional structural evidence supporting the role of cell fusion and cellular reorganization in adaptive responses to nanoradiotherapy.

Supporting Movies

Movie 1. Three-dimensional fluorescence microscopy imaging of B16F10 cells treated with OSAu/PEI on day 2.

B16F10 cells were treated with 11, 33, or 100 μg/mL OSAu/PEI (nanoparticles; green). Merged three-dimensional fluorescence microscopy images of cells stained with Hoechst (nuclei; blue) and TMRE (mitochondria; red) show that OSAu/PEI extensively associated with the cell surface. Merged Z-stack images further reveal internalization of OSAu/PEI into the cells, including fluorescence signals located between mitochondrial regions and along intracellular structures. This movie complements Figure 2 and illustrates the widespread but heterogeneous cellular association of OSAu/PEI. In addition to surface coverage, intracellular localization patterns suggest that OSAu/PEI is positioned to influence both membrane-associated and intracellular responses after irradiation.

Movie 2. Long-term time-lapse fluorescence microscopy imaging of nanoirradiated B16F10 cells.

Time-lapse fluorescence microscopy imaging was carried out up to day 11 using nonirradiated cells and irradiated cells without nanoparticle treatment or treated with 20 μg/mL Au-PEI or 100 μg/mL OSAu/PEI. The movies illustrate differences in cell proliferation, morphology, and TMRE fluorescence over time at low (A) and high (B) magnification. Nonirradiated cells continued to proliferate and formed dense aggregates, whereas irradiated cells exhibited reduced proliferation and heterogeneous mitochondrial signals. These movies provide an overview of the dynamic cellular responses underlying the endpoint analyses shown in Figures 4–6. The appearance of enlarged cells and cells with persistent TMRE fluorescence further indicates that irradiation-induced responses extend beyond uniform cell killing.

Movie 3. Three-dimensional fluorescence microscopy imaging of irradiated B16F10 cells treated with OSAu/PEI on day 5.

B16F10 cells were treated with 100 μg/mL OSAu/PEI (green), irradiated on day 2, and observed under a fluorescence microscope on day 5. A merged three-dimensional movie showing the sequential overlay of nuclear, mitochondrial, and nanoparticle-associated fluorescence clearly demonstrates the presence of OSAu/PEI both within the cytoplasm and on the surface of the polyploid giant cancer cell stained with Hoechst (nuclei; blue) and TMRE (mitochondria; red) (corresponding to Figure 7A, cell b). The Z-stack movie further reveals circular intracellular nanoparticle accumulation adjacent to the nucleus, as well as distribution along the cell surface. These observations support the intracellular and perinuclear localization patterns described in

Figure 7A. The overall signal distribution is consistent with extensive nanoparticle association with enlarged stress-responsive cells after nanoirradiation.

Movie 4. Time-lapse single-cell imaging of irradiated B16F10 cells following nanoradiosensitization with OSAu/PEI.

Nanoirradiated B16F10 cells stained with TMRE were observed by long-term time-lapse imaging, followed by staining with DAPI (yellow) and subsequently Hoechst (cyan) at the indicated time points. Representative events corresponding to Figure 7B1–B5 are shown.

(A) Formation and death of senescent cells and polyploid giant cancer cells (PGCCs) (corresponding to Figure 7B1).
Nuclear enlargement became evident at approximately 3 d 12 h after irradiation, and marked nuclear expansion was observed by day 5. Two senescent cells subsequently disappeared on 10 d 0 h and 10 d 11 h after a transient increase in TMRE fluorescence. Other cells exhibited senescence-associated morphology by 7 d 2 h and later became multinucleated by 9 d 15 h. One senescent cell divided at 9 d 15 h, giving rise to two multinucleated daughter-like cells. One of these cells later disappeared, and its nucleus was DAPI-positive at 11 d 2 h, indicating cell death. Two additional multinucleated cells showed strong TMRE fluorescence but weak or absent nuclear staining at 11 d 2 h–11 d 4 h. These observations indicate that nanoirradiation induced both prolonged senescence-associated remodeling and subsequent death or persistence of PGCC-like cells.

(B) Formation of a PGCC via fusion between normal-sized cells (corresponding to Figure 7B2).
Two normal-sized cells with strong motility and intense TMRE fluorescence approached one

another by day 5 and fused at approximately 7 d 15 h. By 8 d 0 h, they had formed a connected multinucleated structure with persistent TMRE fluorescence and strong Hoechst-associated signals. A spindle-shaped cell showing strong TMRE fluorescence but lacking detectable nuclear staining was also visible at 8 d 0 h. This sequence provides direct temporal evidence that fusion between morphologically nonsenescent cells can generate multinucleated giant cells after nanoirradiation.

(C) Formation of a PGCC via fusion between a senescent cell and surrounding normal-sized cells (corresponding to Figure 7B3).

A senescent-like enlarged cell became evident after day 5. By approximately 8 d 6 h, multiple normal-sized cells had accumulated around this enlarged cell. Fusion between the senescent-like cell and its neighboring cells became evident by 9 d 13 h, and a PGCC containing nuclei of different sizes and fluorescence intensities was visible at 10 d 21 h. This sequence suggests that enlarged senescent-like cells can act as fusion hubs for the formation of multinucleated giant structures.

(D) Emergence of newly formed cells with potential stress-tolerant progeny-like phenotypes after nanoirradiation (corresponding to Figure 7B4).

A spindle-shaped cell became senescent-like after 5 d 10 h, showed increased TMRE fluorescence at 7 d 4 h, and underwent division at approximately 7 d 23 h. The daughter-like cell structures subsequently showed distinct morphologies. One developed into a larger abnormal multinucleated structure and disappeared by 10 d 19 h, whereas the other remained as a smaller morphologically intact cell-like structure with detectable TMRE fluorescence at 10 d 21 h. This event suggests the possible emergence of morphologically distinct daughter-like structures from enlarged or abnormal precursor cells.

(E) Formation and intercellular transfer of mitovesicles mediated by tunneling nanotubes (corresponding to Figure 7B5).

A spindle-shaped cell extended a TMRE-positive tunneling nanotube at 4 d 22 h, indicating active mitochondrial transport. This nanotube ruptured at 5 d 18 h, producing four TMRE-positive vesicle-like bodies. By 6 d 23 h, three of these bodies had become associated with a neighboring cell through a nanotube-like protrusion, and transfer into the recipient cell was observed during approximately 7 d 0 h–7 d 6 h. The donor cell later showed nuclear staining consistent with cell death at 7 d 22 h, whereas the recipient cell remained morphologically intact. These observations support nanotube-associated transfer of mitochondria-containing vesicle-like structures between cells after nanoirradiation.

Taken together, these long-term time-lapse recordings demonstrate that nanoirradiated melanoma cells undergo highly dynamic and heterogeneous responses, including senescence-associated enlargement, multinucleation, fusion between multiple cell types, formation of PGCCs, emergence of smaller surviving progeny, and tunneling nanotube-associated transfer of mitochondrial material.

Movie 5. X-ray computed tomography (CT) analysis of a tumor-bearing mouse following X-ray irradiation.

The hind legs of mice were subcutaneously implanted with B16F10 cells pretreated with 100 μg/mL OSAu/PEI on day 0, followed by irradiation of only the right leg at 10 Gy one day after implantation. This experiment was performed as an additional condition-evaluation study at a

different irradiation dose from that used in the main in vivo experiment shown in Figure 8 (6 Gy), and is presented here to illustrate nanoparticle retention and CT visibility under a more strongly growth-suppressive condition. Both hind legs were imaged using X-ray CT on days 1 and 12. The movie illustrates nanoparticle-associated CT signals in the tumor-bearing hind limbs and shows retention of the signal in the irradiated, growth-suppressed tumor tissue. These data support the theranostic potential of OSAu/PEI described in Figure 8 and Figure S10. The persistent CT signal in the irradiated tumor-bearing limb is consistent with retention of nanoparticle-containing tumor tissue after treatment.